




**Persistent polar distortions from covalent interactions in doped BaTiO<sub>3</sub>**Daniel Hickox-Young , Danilo Puggioni , and James M. Rondinelli \**Department of Materials Science and Engineering, Northwestern University, Evanston, Illinois 60208, USA*

(Received 13 May 2020; revised 1 July 2020; accepted 6 July 2020; published 23 July 2020)

The discovery of polar metals, bulk band conductors which combine broken inversion symmetry and metallic conductivity, has disrupted the long-standing assumption that polar order and metallicity are incompatible. Despite recent progress, however, the circumstances which allow for this property convergence remain ambiguous. Here, we perform a first-principles analysis of the evolution in the polar distortions in perovskite BaTiO<sub>3</sub> under electrostatic doping to ascertain the dependencies of acentricity and electrical conductivity at the microscopic level. We focus on the role of local off-centering displacements, driven by the second-order Jahn-Teller effect, rather than discussing bulk homogeneous and cooperative lifting of inversion symmetry, which relies on long-range Coulombic interactions. We show that *n*-type doping disrupts the Ti-O covalent bond and advocate for using chemical bonding arguments as a framework for understanding the interplay between local distortions and free charge carriers rather than solely principles of dielectric screening in metals. In the process, we develop several tools and electronic descriptors that we expect could enable a more direct comparison between the behavior of doped ferroelectrics, such as BaTiO<sub>3</sub>, and polar metals, such as LiOsO<sub>3</sub>, helping us to better understand their similarities and differences under external perturbation.

DOI: [10.1103/PhysRevB.102.014108](https://doi.org/10.1103/PhysRevB.102.014108)**I. INTRODUCTION**

The traditional framework for understanding polar displacements pitted long-range dipole-dipole interactions (which favor coordinated off centering active in dielectrics) against short-range repulsive forces (which favor high-symmetry structures) [1]. This framework is consistent with a large body of experimental and theoretical literature [2–5], confirming the importance of long-range interactions in stabilizing polar distortions. Such a model implies that high electrical conductivity should be fundamentally incompatible with polar structures since the free charges screen long-range Coulombic interactions. Indeed, this appeared to be the case until the synthesis of the first polar metal LiOsO<sub>3</sub> in 2013 [6].

Although the existence of polar metals was hypothesized as early as 1965 [7], interest in such materials did not begin in earnest until after 2013. Since then, many additional polar metals were proposed and discovered [8–12], leading to a reexamination of the prototypical proper ferroelectric BaTiO<sub>3</sub> under doping as a means to study the interplay between polarization and carrier-controlled metallicity. Considered a prime example, *n*-type doping has consistently been shown to stabilize the cubic phase of BaTiO<sub>3</sub> [2–4, 13]. However, recent work suggests that this preservation of inversion symmetry occurs above the threshold required to screen long-range dipole-dipole interactions [13–16], implying a more complex relationship among the charge carriers, the electronic bands they occupy, and the microscopic structural distortion mechanisms leading to inversion lifting in *d*<sup>0</sup> compounds.

In this paper, we present a first-principles analysis of the polar distortions in BaTiO<sub>3</sub> under *n*-type doping and *p*-type

doping. Although long-range dipole-dipole interactions are clearly important for stabilizing cooperative displacements over the nanoscale and micronscale lengths that result in long-range polar order, we focus on the local off-centering mechanisms within a TiO<sub>6</sub> octahedron. We consider the impact of electrostatic doping through its influence on the second-order term of an expansion of the total energy *E* of a material with respect to distortions *Q* from a high-symmetry (cubic) configuration, otherwise known as the second-order Jahn-Teller effect (SOJT) [17–19],

$$E = E^{(0)} + \langle 0 | \mathcal{H}^{(1)} | 0 \rangle Q + \frac{1}{2} \left[ \langle 0 | \mathcal{H}^{(2)} | 0 \rangle - 2 \sum_n \frac{\langle 0 | \mathcal{H}^{(1)} | n \rangle^2}{E^{(n)} - E^{(0)}} \right] Q^2 + \dots \quad (1)$$

The  $|0\rangle$  and  $|n\rangle$  refer to the ground and excited states, respectively. The first-order term,  $\langle 0 | \mathcal{H}^{(1)} | 0 \rangle Q$ , describes the first-order Jahn-Teller effect and is driven by orbital degeneracy. This term is reduced to 0 in *d*<sup>0</sup> compounds and will not be the focus of our discussion. In the second-order term,  $\langle 0 | \mathcal{H}^{(2)} | 0 \rangle$  is a diagonal matrix element referring to a coordinated displacement in unit cells throughout the crystal, akin to an elastic restoring force. This term (also described as the nonvibronic coupling term) is always greater than zero and, therefore, always repulsive, stabilizing the high-symmetry structure (*Q* = 0). The summation in Eq. (1) describes the mixing of ground and excited states (covalent interactions). It is exclusively a short-range interaction and favors off-centering (*Q* ≠ 0), provided the symmetry of the low-lying energy states is appropriate so that  $\langle 0 | \mathcal{H}^{(1)} | n \rangle$  is nonzero. It is this second-order term which provides the framework for our analysis.

Rather than calculate the second-order term directly (by calculating the Hamiltonian matrix at several distortion

\*jrondinelli@northwestern.edu

amplitudes for each doping level and using finite differences to find the first and second derivatives of each element of the Hamiltonian), we pursue a less labor-intensive approach that can be broadly applied to more complex (multiband) materials. We examine the evolution of several atomic- and electronic-structure-level metrics under carrier doping, defined below, that approximate the components of the second-order term. Namely, we use the Wigner-Seitz radius ( $r_s$ ), force-constant matrix, band-edge energy differences, and crystal orbital Hamiltonian population (COHP) analysis. These metrics can be computed with relatively low human effort and with minimal computational resources (especially since all but the force constants can be computed using the output of a single point total energy calculation, e.g., a density functional theory calculation). In addition, each metric relates intuitively to the changes in chemical bonding and we expect them to transfer to the study of the local bonding environment in other materials, such as polar metals, where delocalized descriptions are used and the features of dielectrics can be difficult to transfer. We also validate findings obtained with these metrics by comparing to results derived from computing maximally localized Wannier functions (MLWFs), which provide accurate local descriptions of electronic structure in both metals and insulators using a different basis (i.e., Wannier functions) than our density functional theory calculations (which use a plane-wave basis) [20].

Applying this suite of metrics to BaTiO<sub>3</sub>, we find that, under  $n$ -type doping, we populate the Ti  $d$  orbitals, shifting the configuration from  $d^0$  to  $d^x$  where  $0 < x < 1$ . As the Ti  $d$ -orbital occupation becomes nonzero, the orbital overlap decreases, reducing the strength of the covalent bond and the magnitude of the SOJT effect [21]. This reduction in orbital overlap is a gradual process, not taking place until surpassing a carrier density associated with modest electrical conductivity, in line with recent experiments [13–15]. Meanwhile, under  $p$ -type doping, we find that the states near the valence-band edge do not participate in the covalent bond, and so the polar distortion persists more or less unaffected (if not slightly enhanced). This circumstance is much more difficult to achieve through chemical substitution or interstitial defects than electron doping, and so is unlikely to be realized in experiment, but the contrast with electron doping helps support this analysis and may lead to fruitful comparisons to other systems. In addition to the impact of doping on the orbital overlap (which we view as the dominant effect controlling the persistence of the polar distortion under doping), we observe a charge self-regulation effect driven by an increase in the band gap. This increase in energy difference  $E^{(n)} - E^{(0)}$  [the denominator of the covalent bonding term in Eq. (1)] has a minimal effect on the magnitude of the SOJT effect but serves to explain the organization of charge in the unit cell upon doping.

## II. MATERIALS AND METHODS

### A. BaTiO<sub>3</sub> as a model material

BaTiO<sub>3</sub> undergoes a series of ferroelectric transitions. Beginning with the high-temperature cubic perovskite ( $Pm\bar{3}m$ ) phase, the Ti cation off-centers upon cooling to produce

the tetragonal ( $P4mm$ ), orthorhombic ( $Amm2$ ), and rhombohedral ( $R3m$ ) phases in succession [22]. In this paper, we are concerned with the mechanisms which lift inversion symmetry, so we focus exclusively on the cubic-tetragonal transition which exhibits the fewest atomic displacements necessary to break parity. This transition occurs at  $\approx 400$  K. The tetragonal-orthorhombic transition occurs around 280 K, which makes the tetragonal  $P4mm$  phase stable at room temperature.

### B. Density functional theory

We perform first-principles calculations using density functional theory (DFT) as implemented in the Vienna *ab initio* simulation package (VASP) [23,24] using a plane-wave basis set with a 800-eV energy cutoff. The Perdew-Burke-Ernzerhof (PBE) exchange-correlation functional revised for solids (PBEsol) [25] was used along with the projector-augmented wave method to treat the separation of the core and valence electrons [26]. Lattice parameters, volume, and atomic positions were relaxed in various combinations (as specified) such that the forces and stress tensor were converged to  $5 \times 10^{-4}$  eV  $\text{\AA}^{-1}$  and  $2 \times 10^{-3}$  eV  $\text{\AA}^{-2}$ , respectively. The Brillouin zone was sampled using a  $7 \times 7 \times 7$  Monkhorst-Pack mesh and the tetrahedron method. Using these parameters, we find our relaxed structures are in good agreement with both experiment and other choices of density functionals (Table I).

### C. Carrier doping

We assess the evolution of the inversion symmetry-breaking transition with changes in carrier type and density by artificially varying the number of electrons in the system (by fractional amounts) while applying a compensating background charge to retain charge neutrality. This approach allows us to change the orbital filling without introduction of additional chemical species that would introduce secondary atomic distortions. This also allows us to simulate dilute levels of doping without increasing the size of the unit cell as would be required for modeling heterovalent substitution of  $A^{3+}$  or  $A^{1+}$  cations on the Ba sublattice. Although not without its drawbacks, this method is frequently used to simulate doped FEs [4,16,32] and shown to provide accurate structure-property descriptions. The primary carrier concentrations examined range from 0.05 electrons (or holes) per unit cell (u.c.) to 0.20 electrons (or holes) per u.c., which correspond to  $7.9 \times 10^{20}$  and  $3.2 \times 10^{21}$  cm<sup>-3</sup>, respectively.

### D. Lattice dynamics

Phonon frequencies were computed using the frozen phonon method after relaxation of the atomic positions, cell shape (i.e., the degree of tetragonality), and sometimes volume (as indicated below). Phonon calculations were prepared and analyzed using the PHONOPY software package [33]. We find that our calculations of the  $\Gamma$ -centered phonon modes are consistent with both previous computational and experimental studies (Table I) and that their dispersions throughout the Brillouin zone match previous studies (Fig. 1). Evidence of each of the three successive ferroelectric phase transitions is

TABLE I. A comparison of several methods (both simulation and experiment) as applied to the study of cubic BaTiO<sub>3</sub>, where  $a$  is the lattice parameter,  $V$  is the volume,  $E_g$  is the band gap, and the remaining columns are  $\Gamma$ -point phonon frequencies in cm<sup>-1</sup>. LDA, PBE, and SCAN refer to the local-density approximation, Perdew-Burke-Ernzerhof, and strongly constrained and appropriately normed density functionals, respectively.

Method	$a$ (Å)	$V$ (Å <sup>3</sup> )	$E_g$ (eV)	$T_{1u}$ (TO1)	$T_{1u}$ (TO2)	$T_{2u}$ (silent)	$T_{1u}$ (TO3)
Experiment	4.01 [27]	64.29 [27]	3.2 [28]	Soft [29]	182 [29]	306 [29]	482 [29]
DFT-LDA (Ref. [5])	3.94	61.16	1.84	113i	184	288	481
DFT-PBE (Ref. [30])	4.04	65.74	1.9	240i	175	290	460
DFT-SCAN (Ref. [31])	4.003	64.14	2.13 <sup>a</sup>	220i	183	290	476
DFT-PBEsol (This paper)	3.98	63.25	1.79	201i	178	288	465

<sup>a</sup>Reported only for the tetragonal phase, which tends to exhibit band gaps 0.1–0.2 eV larger than the cubic phase.

apparent when assessing the lattice dynamical stability of the cubic phase. However, we focus on the dynamics of the Slater mode at  $\Gamma$  (circled in Fig. 1), which drives the transition to the tetragonal phase. Evidence of the stabilization of soft modes throughout the Brillouin zone under each phase transition is provided in Fig. S1 of Ref. [34].

Force constants are computed using density functional perturbation theory, generating a  $3N \times 3N$  matrix where  $N$  is the number of atoms in the unit cell. Force constants are calculated using the expression,

$$\phi_{ij} = \frac{\delta^2 E}{\delta u_i \delta u_j}, \quad (2)$$

where  $E$  is the total energy,  $\delta u_{i,j}$  are small atomic displacements ( $\approx 0.015$  Å), and  $\phi_{ij}$  are the resulting force constants for the relative motion of atoms  $i$  and  $j$ . The elements of the force constant matrix on the diagonal ( $i = j$ ) are the self-force constants (SFCs), corresponding to the second derivative of the energy with respect to the displacement of the atom. Thus, a negative (positive) value of the SFC along the diagonal indicates an energy gain (cost) upon displacement of the atom. Off-diagonal elements ( $i \neq j$ ) correspond to the energy derivative with respect to the relative motion of two different atoms, equivalent to an effective spring constant and termed the interatomic force constants (IFCs). Because the motion of the atoms is relative to one another,  $\delta u_i$  and  $\delta u_j$  have opposite signs. Thus, a negative (positive) IFC indicates an energy cost (gain) when those atoms displace relative to one another.

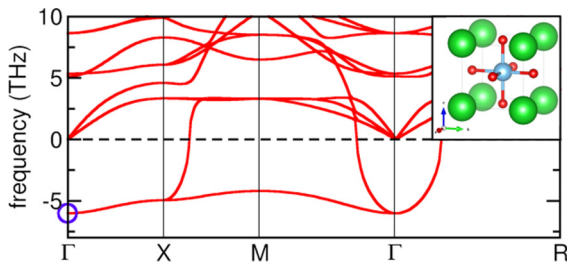


FIG. 1. Phonon dispersions for cubic ( $Pm\bar{3}m$ ) BaTiO<sub>3</sub>. The Slater mode, responsible for driving the ferroelectric transition to the tetragonal ( $P4mm$ ) phase is circled. (inset) Unit cell for cubic BaTiO<sub>3</sub>.

## E. Electronic structure

Our calculations of the electronic structure for  $P4mm$  BaTiO<sub>3</sub> demonstrate the expected insulating behavior, featuring a valence band (VB) (dominated by O  $2p$  orbitals) separated from a conduction band (CB) (dominated by Ti  $3d$  states) by a band gap of about 1.8 eV (Fig. 2). This is consistent with previous theoretical studies in that it underestimates the band gap by  $\approx 1.4$  eV (Table I). Although we expect some  $pd$  hybridization from ligand-field theory as found from the projected DOS shown in Fig. 2(a), we further quantify this interaction by computing the COHP. The COHP is determined by weighting the electronic DOS by the Hamiltonian elements corresponding to orbital overlap, which we perform using the LOBSTER code [35–38]. The result is a method of energy partitioning the DOS into bonding, nonbonding, and antibonding regions. These are generally identified by plotting the COHP projected onto a particular atomic (or orbital) pair (pCOHP). The convention is to plot the negative pCOHP ( $-pCOHP$ , which is unitless) so that bonding interactions are positive whereas antibonding interactions are negative. Figure 2 confirms our expectation and provides significantly more details, allowing us to

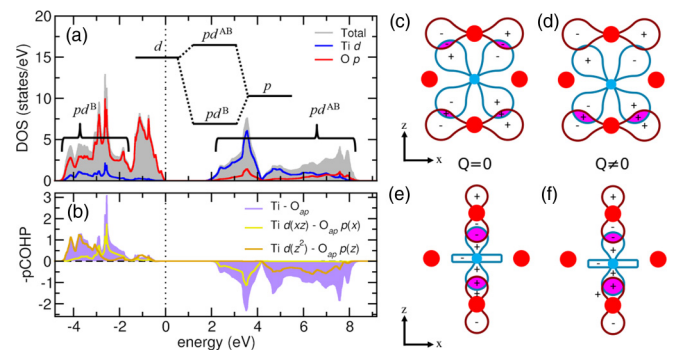


FIG. 2. (a) Electronic density of states (DOS) for tetragonal BaTiO<sub>3</sub> with a molecular orbital diagram illustrating the covalent bonding between Ti and O. (b) Projected crystal orbital Hamiltonian population (pCOHP) for tetragonal BaTiO<sub>3</sub>. (c)–(f) Illustration of the enhanced overlap under polar distortion  $Q$  along the  $z$  axis driven by the SOJT effect, shown for both (c) and (d)  $\pi$  bonding between Ti  $d(xz/yz)$  and O  $p(x/y)$  and (e) and (f)  $\sigma$  bonding between Ti  $d(z^2)$  and O ( $p_z$ ). In the cubic structure, (c) and (e), the net overlap is 0 by symmetry but becomes nonzero after the distortion as shown in (d) and (f).

differentiate between  $\pi$  bonding [overlap of Ti  $d(xz)$  and  $O_{ap} p(x)$ , which drives the transition] and  $\sigma$  bonding [Ti  $d(z^2)$  and  $O_{ap} p(z)$ , also strengthened under the transition], which will be exploited below in our analysis.

Maximally localized Wannier functions represent an alternative route to quantifying changes in chemical bonding. Using the WANNIER90 code [39], we compute the evolution in the real-space wave functions of  $\text{BaTiO}_3$  under electron doping. In particular, we use the VASP-WANNIER90 interface [40], choosing to project onto the O  $2p$  and Ti  $3d$  orbitals.

### III. RESULTS

#### A. Charge redistribution upon electron doping and hole doping

Here, we focus on the bond between Ti and O atoms, described by the covalent bonding term in Eq. (1), upon adding charge carriers into tetragonal  $\text{BaTiO}_3$ . To track the charge associated with a path in real space between Ti and O, we use the Wigner-Seitz radius, defined as

$$r_s = [3/(4\pi n)]^{1/3}, \quad (3)$$

which corresponds to the radius of a sphere whose volume contains one electron of charge, obtained from our DFT charge density. Large values of  $r_s$  indicate low-density regions, which tend to correspond to interstitial sites between atoms where little chemical bonding occurs. Small values of  $r_s$  occur near atomic sites or along more covalent bonds. We prefer  $r_s$  to charge density in this analysis because  $r_s$  provides a rigorously defined method of attributing charge to a path in real space and allows us to quantitatively compare different materials and doping configurations. Further evidence of the utility of this descriptor is provided in Fig. S2 of Ref. [34].

Without any additional carriers in tetragonal  $\text{BaTiO}_3$ , we find a smaller peak along the shorter Ti-O bond [Fig. 3(a)] than along the long bond, indicating stronger covalent bonding and weaker covalent bonding, respectively. This enhanced bonding of the shorter Ti-O bond is driven by orbital overlap [Figs. 2(c)–2(f)] as described by the SOJT effect. Both  $\sigma$  and  $\pi$  bonds contribute here, although it is the  $\pi$  bond which dominates (due to the smaller energy difference between bonding states) and acts to stabilize the breaking of inversion symmetry by Ti off-centering. To understand how doping affects the charge distribution, we first plot  $\Delta r_s$  as a function of doping in tetragonal  $\text{BaTiO}_3$  with the volume and atomic positions held constant. We keep fixed the Ti-O bond length to separate the role of dielectric screening from electronic screening. Here, we find an asymmetry between electron doping and hole doping in terms of the changes in local bonding. Whereas, under electron doping, we find a clear increase in  $r_s$  (decrease in charge density) near Ti and decrease (increase in charge density) near O along both bonds, under hole doping, the trend is much less continuous and appears to both occur only along the long Ti-O bond and with smaller magnitude ( $\approx 1 \times 10^{-3}$  vs  $\approx 1.5 \times 10^{-3}$  Å). We attribute this difference in response to the difference in the bonding character of the dopant states [Fig. 2(b)].  $n$ -type doping immediately begins to populate antibonding states, directly impacting states related to the hybridization between Ti and O, whereas  $h$ -type doping

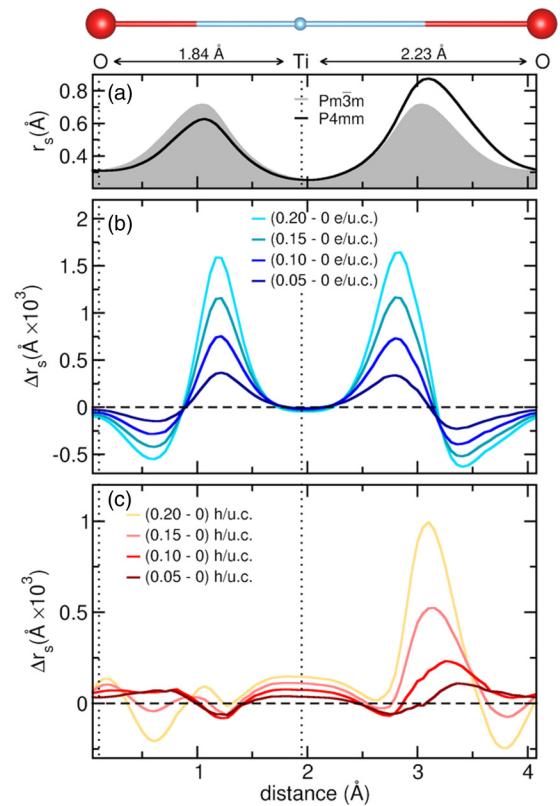


FIG. 3. (a) Wigner-Seitz radius ( $r_s$ ) calculated on a path through the center of the relaxed  $\text{BaTiO}_3$  unit cell (cubic and tetragonal) along the axial Ti-O bond. The change in  $r_s$  along the same path in the tetragonal unit cell under (b) electron doping and (c) hole doping with the lattice parameters and atomic positions fixed to those of the relaxed (undoped) tetragonal unit cell.

initially empties nonbonding states, thereby having a minimal effect on the sharing of electrons along the Ti-O bond.

In both cases, however, there appears to be a net motion of charge away from Ti and towards O. Although this might appear counterintuitive, a similar transfer of charge has been proposed to occur upon doping oxide semiconductors; it is described as charge self-regulation [41]. The addition of electrons (holes) shifts the conduction band to higher energy (valence band; lower energy), causing the predominantly empty cation states to take on greater antibonding character whereas the filled anion states take on greater bonding character. Since the bonding states are filled and the antibonding states are only partially occupied, this results in an effective increase in the number of electrons associated with the anions. We appear to observe a similar effect; the addition of electrons (holes) into the Ti-dominated conduction band (O-dominated valence band) results in a shift of electronic charge away from Ti and toward O. As mentioned above, however, the effect is more pronounced under electron doping since  $n$ -type carriers immediately populate states that participate in the Ti-O bond whereas  $h$ -type carriers do not. If electrons and holes affect the Ti-O bond (the driving force behind the SOJT effect) in different ways, we should expect that the response of the polar distortion under electron doping and hole doping will be asymmetric as well.

### B. Doping effects on the polar distortion

To evaluate the consequences of this charge distribution on the crystal structure, we consider both structural metrics and quantitative assessments of the driving force towards the polar distortion itself. The evolution of the polar distortion under electron doping has been studied previously computationally and experimentally, finding that the high-symmetry phase is stabilized with a carrier concentration of  $\sim 1.7 \times 10^{21} \text{ e/cm}^3$  ( $0.11 \text{ e/u.c.}$ ) [4,13]. This contraindication between electron charge carriers and broken inversion symmetry is consistent with traditional frameworks describing the stabilization of polar modes via long-range Coulombic interactions. However, the traditional framework begins to break down when you compare the threshold for stabilization to the threshold for metallic conductivity [13,15], achieved at  $\sim 10^{20} \text{ cm}^{-3}$  (as determined by the carrier concentration required to make  $\delta\rho/\delta T > 0$ ). The experimental value aligns well with the Mott criterion for conductivity ( $n_c^{1/3} a_0 \approx 0.25$ ), a carrier concentration of approximately  $2.4 \times 10^{20} \text{ cm}^{-3}$ .

It appears that *n*-type dopants induce metallicity at a concentration one order of magnitude lower than that required to turn off the polar distortion. Attempts have been made to argue that metallicity is achieved prior to the necessary reduction in screening length [4], but this has been refuted by recent theoretical work [16]. In addition, a screening length argument fails to account for the differences under hole doping.

When doping with holes, the stabilization occurs much more gradually; counterintuitively, the polar distortion is enhanced for small hole concentrations (Fig. 4). This difference in behavior depending on the sign of the charge carriers has been observed via theoretical methods before [16], although, to our knowledge, never observed in experiment owing to the challenges in hole-doping  $\text{BaTiO}_3$ . If long-range, Coulomb-type interactions were the sole stabilizing mechanism in polar materials, we would expect a comparable carrier density to produce a similar screening effect, regardless of the sign of the charge. The divergent behavior of the two regimes (especially at low concentrations) indicates that the stabilizing effect of short-range off-centering mechanisms must also be accounted for, if not prioritized, when examining how metallicity and acentricity interact.

These results support the use of the SOJT effect as a framework for our analysis and provide preliminary insight into the impact of doping as the magnitude of the polar distortion is closely related to the distortion magnitude  $Q$  from Eq. (1). The sign of the coefficient of the second-order term (the value in square brackets) determines whether this distortion is energetically favorable, resulting from the competition between covalent bonding and the rigidity of the lattice. If the distortion amplitude is greater than zero under doping, then the covalent term remains dominant.

What microscopic mechanisms control this term? Using soft-mode theory, we can approximate the magnitude of the resulting driving force and identify the atoms that play the largest role in stabilizing the distortion. To that end, we next assess the lattice dynamical properties, focusing on the soft Slater mode. Consistent with previous work [1,4,5], we find that the cubic ( $Pm\bar{3}m$ ) phase exhibits an unstable transverse optical phonon mode known as the Slater mode (Fig. 1). The

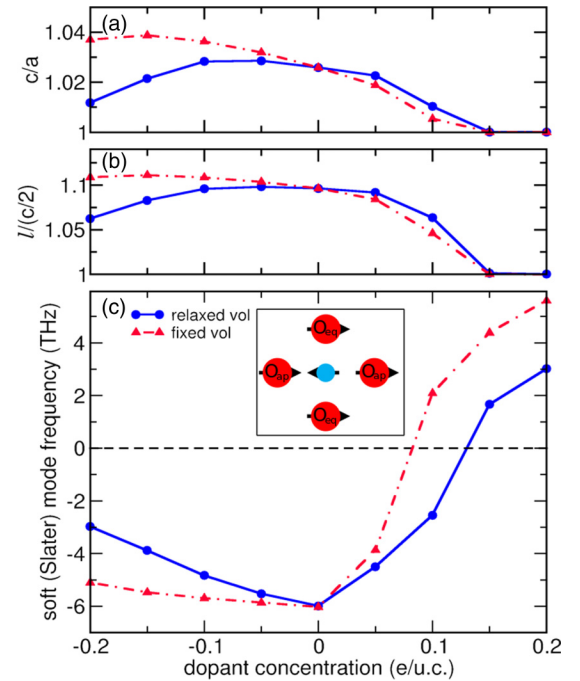


FIG. 4. (a) The axial  $c/a$  ratio and (b) the degree of polar distortion (given by the ratio of the long Ti-O ( $l$ ) bond to half the lattice parameter along the  $c$  axis) of the relaxed tetragonal cell both fixed to the undoped volume and with the volume relaxed as a function of doping. (c) Slater mode (TO1) frequency as calculated for the high-symmetry cubic cell as a function of doping. (inset) Slater mode displacement pattern showing relative motion of Ti and the surrounding O anions.

atomic distortion pattern for this phonon mode [the inset to Fig. 4(c)] breaks the symmetry elements required to drive the transition to the tetragonal phase ( $P4mm$ ) and is dominated by the displacement of Ti and O atoms in opposite directions along one of the three crystallographic axes.

Under doping, the difference in the Slater mode response between electron doping and hole doping is again evident but not as stark as the evolution of the distortion magnitude itself (there is no enhancement of the instability under hole doping). The fully relaxed structure, in particular, exhibits a surprisingly large shift in frequency under hole doping, but comparison with the fixed volume case reveals that this is largely due to volume effects. Hole (electron) doping reduces (increases) the volume thereby disfavoring (favoring) the polar distortion. Focusing on the fixed volume case, we see that, as before, hole doping has a muted effect on the soft mode, whereas electron doping rapidly stabilizes the phonon mode. This corroborates our analysis of the relaxed tetragonal structure, confirming that the driving force for displacement responds differently to electron doping and hole doping.

There remains a subtle difference between the Slater mode evolution and the polar distortion magnitude [the Slater mode frequency increases monotonically under hole doping whereas  $l/(c/2)$  increases then decreases] for which we do not have a conclusive explanation. However, we hypothesize that this arises from changes in the DOS at the valence-band edge. In the cubic structure, all oxygen sites are related by

symmetry and their  $p$  states are degenerate. Thus, in the cubic phase,  $h$ -type doping affects all O sites equally, whereas, in the tetragonal phase, the  $O_{ap}$  sites are shifted to lower energy (see Fig. S3 in Ref. [34]) so that  $h$ -type doping initially affects only the  $O_{eq}$  sites, which do not participate in the short bond supporting the SOJT effect. The polar distortion itself also enhances the degree of covalency, further shifting the bonding states to lower energy. These shifts in energy are small, but may be enough to subtly alter the impact of hole doping in the cubic and tetragonal structures.

In order to more directly probe the changing dynamical contributions from individual atoms, we also analyzed the force constants under both electron doping and hole doping (as shown in Fig. S4 in Ref. [34]). We found that the force constants describing the local off-centering of Ti and relative displacement of Ti and  $O_{ap}$  (apical O atom) saw the greatest change, rapidly stiffening under electron doping and hardening more gradually under hole doping, following the pattern in Fig. 1. This result supports our assessment that changes in the local environment of Ti and  $O_{ap}$  are responsible for the stabilization of the cubic structure as well as the differences in the response of the structure under electron doping and hole doping.

### C. Electronic structure effects

The band structure of pristine  $\text{BaTiO}_3$  exhibits a valence band consisting of O-dominated bonding states and a conduction band of Ti-dominated antibonding states, separated by a gap of about 1.9 eV at the DFT-generalized gradient approximation (-GGA) level. The energies of these states appear in the denominator of the covalent-bonding term in Eq. (1), specifically the energy difference between the ground and the excited states.

We next assess the evolution of this energy difference by calculating the electronic structure of  $\text{BaTiO}_3$  under doping (Fig. 5). To account for changes in the absolute energy caused by altering the number of charge carriers (and the corresponding neutralizing background charge), the listed band-edge energies are determined relative to the O  $2s$  semicore-level states. Here, we find evidence of the charge self-regulation effect. The conduction-band edge shifts to higher energy under electron doping, whereas the valence-band edge shifts to lower energy under hole doping (Fig. 5). This shift in the energy of Ti and O states, respectively, leads to a change in character of the resulting molecular orbitals. The antibonding states acquire greater Ti character whereas the bonding states take on greater O character. Since the bonding states are much more occupied than the antibonding states, charge effectively moves from the Ti site to the ligands, consistent with our observations of  $\Delta r_s$  (Fig. 3).

We also plot the energy difference between the highest occupied O  $p$  states and the lowest unoccupied Ti  $d$  states ( $E_1$ ) as well as the band-gap ( $E_2$ ) under doping (Fig. 5). We find a significant increase in both differences under both doping directions, which can largely be attributed to charge self-regulation. The changes in  $E_1$  and  $E_2$  exhibit a slight asymmetry in favor of electron doping, but the response under hole doping comes closer to mirroring the electron case than in any of our other metrics. This energy shift induced by

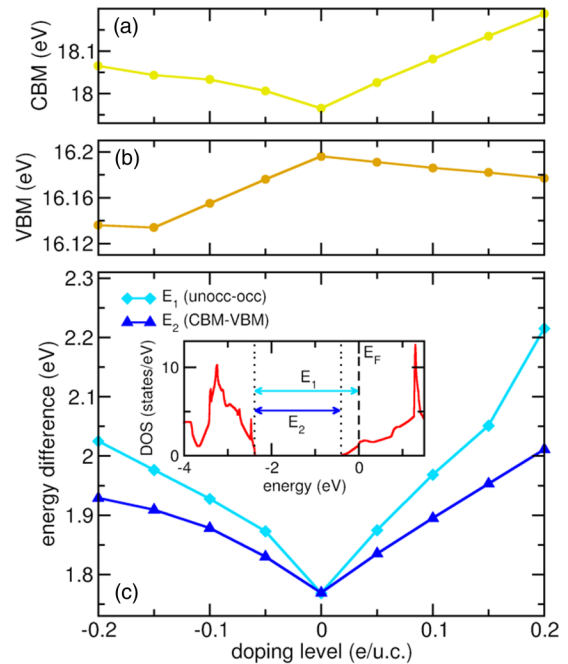


FIG. 5. Evolution of (a) conduction-band minimum (CBM), (b) valence-band maximum (VBM), and (c) energy differences  $E_1$  and  $E_2$  (defined in the inset) under electron doping and hole doping in tetragonal  $\text{BaTiO}_3$  with lattice parameters and atomic positions held constant.

doping drives an increase in the denominator of the covalent-bonding term in Eq. (1) (indicated by  $E_1$ ), reducing the stabilization of the polar displacement by mixing ground and excited states (represented in the numerator). However, the magnitude of this effect is small, if not negligible, since the energy-difference increase under hole doping does not seem to significantly impact the magnitude of the polar distortion (Fig. 2). The underestimation of the band gap by DFT at the GGA level also artificially magnifies the relative change in energy differences, further reducing the expected impact of changes in energy differences on the polar instability in experimental  $\text{BaTiO}_3$  samples. Meanwhile, as will be shown below, the changes in the magnitude of the polar distortion correlate well with changes in the degree of orbital overlap, implying that the covalent-bonding term in Eq. (1) overwhelmingly drives the off-centering mechanism.

### D. Quantifying changes in bonding

To examine changes in covalent bonding more directly, we performed COHP analysis of the Ti- $O_{ap}$  interaction under doping. Since the COHP is calculated using elements of the Hamiltonian corresponding to orbital overlaps, it gives us an approximation of the  $\langle 0|\mathcal{H}^{(1)}|n\rangle$  term in Eq. (1). Although the focus of this paper is on the Ti- $O_{ap}$  interaction, we find evidence that the Ti- $O_{eq}$  interaction is non-negligible and may be worthy of further study (as shown in Fig. S3 of Ref. [34]). By comparing the COHP to the electronic DOS, we find the Ti-dominated CB is, indeed, of primarily antibonding character, whereas the O-dominated VB is primarily of bonding character, consistent with previous work [42] and expected from our molecular orbital analysis (Fig. 2).

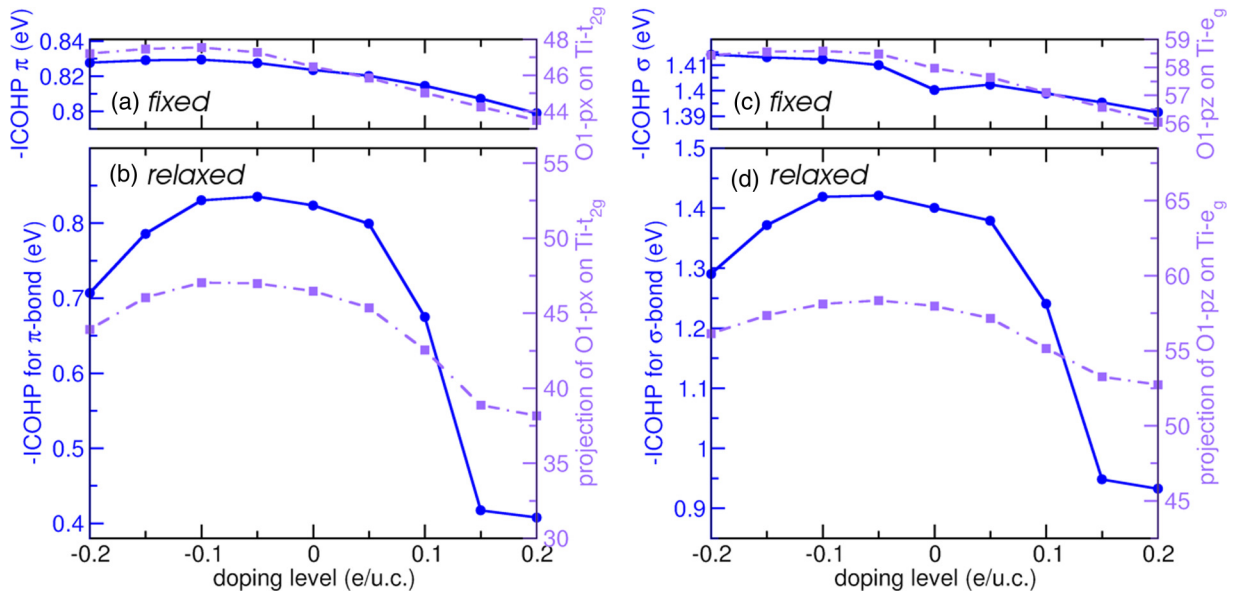


FIG. 6. Carrier doping leads to similar responses in both the integration of the projected crystal orbital Hamiltonian population (ICOHP) up to the Fermi level (circles) and the projection of the  $O_{ap}$  Wannier functions onto the Ti states (squares). Both ICOHP and projection Wannier function data are shown for (a) and (b)  $\pi$  and (c) and (d)  $\sigma$  bonds. The evolution of each quantity under doping is shown for (a) and (c) the unit cell fixed to the undoped relaxed tetragonal phase and for (b) and (d) the fully relaxed unit cells (which initially are tetragonal but become cubic under sufficient electron doping).

Upon electron doping into the CB, we find that even dilute concentrations result in the population of antibonding states. The presence of antibonding states below the Fermi level is an unfavorable configuration, already indicating that electron doping may disrupt the stability of the Ti- $O_{ap}$  bond. At the VB edge, the O states at the top of the band are of nonbonding character, predominately associated with the equatorial O atoms, meaning that a much greater concentration of holes is required to shift the Fermi level into the bonding regime than electrons were required to enter the antibonding regime. This analysis provides some insight as to the asymmetrical response of BaTiO<sub>3</sub> under electron doping and hole doping as it appears that hole-doped states (at least, initially) do not affect the Ti-O interaction. We can discern this behavior more quantitatively by plotting the integrated COHP, summarizing the bonding character by integrating the  $-p\text{COHP}$  from low energy up to the Fermi level (Fig. 6). We perform this analysis for both the  $\pi$  bond between Ti  $d(xz)$  and  $O_{ap}$   $p(x)$  orbitals [related by symmetry to a second  $\pi$  bond between  $d(xy)$  and  $p(y)$  orbitals] and the  $\sigma$  bond between Ti  $d(z^2)$  and  $O_{ap}$   $p(z)$  orbitals, which represent the  $n = 1$  and  $n = 2$  interactions, respectively, in Eq. (1). Note that because we are plotting overlap data for only one of the  $\pi$  bonds contributing to the distortion, one should apply a factor of 2 prior to comparison with the  $\sigma$ -bond data.

Under electron doping, we find the anticipated decrease in bonding character whereas, under hole doping, there appears to be a slight strengthening of the Ti- $O_{ap}$  bond, consistent with the enhancement of the distortion shown in Fig. 4. This broad trend is found in both the  $\pi$  and the  $\sigma$  bonds, but the two exhibit notable differences when the volume and positions are held constant to the relaxed undoped tetragonal phase.

Low levels of  $n$ -type doping appear to slightly enhance the orbital overlap for the  $\sigma$  bond when the structure is fixed to the undoped tetragonal phase. This change fails to match any of our previous observations, nor does it align with the response of the  $\pi$ -bond orbital overlap, which immediately and continuously decreases. The  $\sigma$ -bond overlap under  $h$ -type doping (again in the fixed case) also increases more starkly and more monotonically than our other metrics for changes in bonding. These differences imply that the  $\pi$  bond exerts a much greater influence on the SOJT effect and the resulting distortion than the  $\sigma$  bond. This interpretation is corroborated by the energy level of these two interactions as well as their change in magnitude when relaxed under doping.  $\pi$ -antibonding states form the conduction-band edge and are the first to be occupied by electron doping.  $\sigma$ -antibonding states are located at higher energy, reducing the strength of the interaction and moving them beyond the range of  $n$ -type doping. The magnitude of the change in overlap for the two types of bonding under doping of the relaxed structure appears similar, but recall that we only show overlap data for one of two identical  $\pi$  bonds making the overall change much greater in both absolute and proportional terms.

Thus, we conclude that electron doping shifts the Fermi level into an antibonding regime, which immediately disrupts the Ti- $O_{ap}$  bond and reduces the orbital interaction term in Eq. (1). Hole doping initially has little to no effect as the Fermi level passes through nonbonding states until, eventually, the bonding states are impacted, and the covalent bond is again weakened. Whereas both  $\sigma$  and  $\pi$  bonds contribute, it is the  $\pi$ -bonding interaction which exerts the dominant influence on the polar distortion, a conclusion consistent with previous work on the SOJT effect in BaTiO<sub>3</sub> [21].

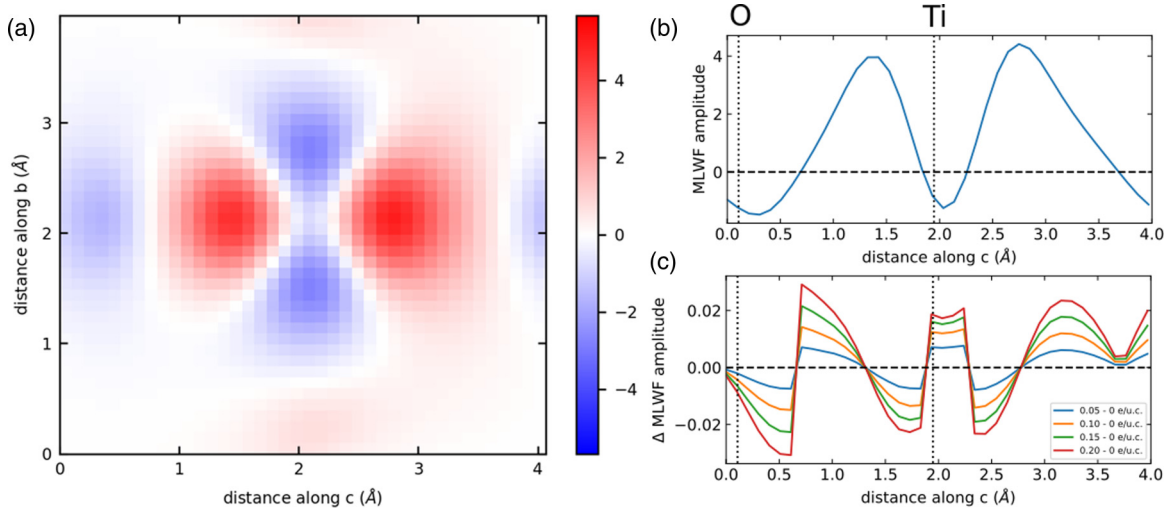


FIG. 7. (a) Two-dimensional slice of the MLWF associated with the Ti- $d(z^2)$  orbital taken perpendicular to the  $a$  axis so that it cuts through the Ti and apical oxygen bond. (b) MLWF amplitude along the apical Ti-O bond. (c) Change in MLWF amplitude as a function of electron doping taken along the same path through the apical Ti-O bond.

### E. MLWFs

We next examine changes in the amplitude of the MLWFs, frequently used to describe chemical bonding, focusing on the MLWF associated with the Ti- $d(z^2)$  orbital [primarily responsible for bonding with the  $O_{ap}$ - $p(z)$  orbital]. Although we previously established that the  $\pi$  bond contributes more to the off-centering of Ti, it is nontrivial to determine a path in real space for analyzing the movement of charge along the  $\pi$  bonds. We have, instead, chosen an orbital that lies along the polar axis as an example for comparing to our previous observations of charge redistribution using  $r_s$  as a metric.

Similar to the  $r_s$  evolution, we find a shift of the amplitude away from the Ti center and towards  $O_{ap}$ , as indicated by shifts in the lobes of the orbital as well as increases in amplitude near oxygen, especially along the long bond [Fig. 7(c)]. Similar shifts are observed in the MLWF associated with the  $O_{ap}$ - $p(z)$  orbital as shown in Fig. S5 in Ref. [34]. As with the  $\Delta r_s$  analysis, we attribute this response, in part, to the charge self-regulation effect.

We can also use MLWFs to approximate the strength of the Ti- $O_{ap}$  covalent bond by computing the projection of MLWFs associated with different O  $p$  orbitals onto Ti states. As with the ICOHP analysis, we do this for both the  $\pi$  [ $O_{ap}$   $p(x)$  projected onto Ti- $e_g$  states] and  $\sigma$  [ $O_{ap}$   $p(z)$  projected onto Ti- $t_{2g}$  states] interactions (Fig. 6). An example of this projection process is shown in Fig. S6 of Ref. [34]. Similar to the evolution of the ICOHP, we find that electron doping decreases the magnitude of the projection, whereas hole doping has a small enhancing effect. This result supports our previous conclusions regarding the impact of doping on the bonding between Ti and apical oxygen. Unlike the ICOHP data, the trends for the  $\sigma$  and  $\pi$  bonds are almost identical, supporting the idea that  $\sigma$  bonding plays a key role in stabilizing the distortion. However, the same considerations regarding the absolute and proportional magnitudes of the changes under doping still apply as these are both much greater for the  $\pi$ -bonding interactions. The differences between the ICOHP data and the MLWF projections can likely be attributed to a

subtle difference in what they measure; ICOHP data use the Hamiltonian element associated with orbital overlap to weight the DOS by bonding character, whereas the MLWF projection is more directly an estimate of the degree of hybridization. Despite their differences, the two methods agree with our main findings; the strength of the covalent bond is the primary driving force behind local off-centering, and the change in this bond strength under doping directly controls the change in off-centering via the SOJT effect.

## IV. DISCUSSION

Each of the metrics employed herein demonstrates the same asymmetric response under electron doping and hole doping, consistent with the assessment that short-range interactions must be responsible (or, at least, essential) for local off-centering. Such an assessment is further corroborated by the growing evidence that polar distortions persist beyond a modest threshold for conductivity [13–15]. A similar observation was made in Ref. [16], not just for BaTiO<sub>3</sub>, but for a variety of ferroelectrics where the short-range interaction was explained using a new concept introduced by the authors as “metascreening.” We restate the concept here succinctly: When a perovskite-structured ferroelectric like BaTiO<sub>3</sub> is doped with free charge carriers, those free charges rapidly distribute themselves in opposition to the local dipole moment generated by Ti off-centering relative to the oxygen octahedron. The reorganization of free charges so as to generate a depolarizing field leads to a high concentration of negative charge carriers near the positively charged Ti<sup>4+</sup> ion and a similar concentration of positive charge carriers near the negatively charged O<sup>2-</sup> ions.

Although this description of the metascreening phenomenon appears to correctly predict the surprising persistence of polar distortions in a metallic environment, we propose an alternative and more intuitive approach. Rather than construct new physics, we explain the same phenomenon by considering the impact of additional charge carriers on the



strength of the covalent bonding between the atoms responsible for driving the local distortion (namely, Ti and O in BaTiO<sub>3</sub>). Conveniently, the covalent-bonding approach also predicts an increased concentration of electrons along the shortened Ti-O bond near the positively charged Ti side of the dipole and a corresponding decrease along the long bond closer to the distorted oxygen octahedron (Fig. 3).

This approach draws on previous analysis of the dominant (and entirely short-range) nature of the SOJT effect. In developing the theory, Polinger *et al.* observed that, whereas force constants can be decomposed into a strongly negative long-range component and a strongly positive short-range component, the SOJT effect accounts for more than 70% of the so-called long-range contribution [21]. Under this framework, the persistence of local off-centering despite metallic screening is unsurprising. Even with a small level of *n*-type carriers, the polar distortion enhances covalency, reducing the energy of the occupied  $O_{ap} p$  orbitals in accordance with Eq. (1).

Why, then, does electron doping eventually favor the high-symmetry state? This occurs through the disruption of the SOJT mechanism. As previously noted in the literature,  $d^1$  perovskites are incapable of exhibiting SOJT-driven distortions due to the differing spin multiplicity between ground and excited states, reducing  $\langle 0|\mathcal{H}^{(1)}|n\rangle$  to zero [19,21,32]. As electrons are added to the  $d^0$  system in BaTiO<sub>3</sub>, the nonzero occupancy of the Ti  $d$  orbitals reduces the magnitude of the enhanced covalency. This eventually changes the sign of the second-order term in Eq. (1) as the rigidity of the lattice (i.e., the elastic nonvibronic coupling term  $\langle 0|\mathcal{H}^{(2)}|0\rangle$ ) dominates, and the high-symmetry structure is restored.

In addition to returning to more familiar physical arguments, we believe the SOJT approach allows us to more precisely accommodate the difference in responses upon electron and hole doping. Electron doping begins to populate antibonding states at the conduction-band edge, leading to charge self-regulation, increased band gap, and, most importantly, disrupting the orbital overlap related to the  $\pi$  bonding between Ti and O, eventually quenching the polar distortion. Hole doping initially populates only nonbonding states, and although we again see a modest charge self-regulation effect and opening of the band gap, the strength of the covalent bond is relatively unchanged if not slightly enhanced. This leads to a slight increase in the polar distortion which only wanes once the *h*-type carriers reach a sufficient concentration to depopulate bonding states and decrease the strength of the bond.

Finally, whereas the metascreening model provides a sufficient explanation for doped conventional ferroelectrics, we

expect that modeling the effect of charge carriers on bonding interactions will be more transferable to discussions of other contexts where the polar distortion mechanism is decoupled from the presence of free charges (e.g., improper ferroelectrics or polar metals). Our analysis is consistent with the so-called “weak-coupling hypothesis” proposed in Ref. [9], which has been extensively utilized to understand the stability of polar metals. Under electron doping, conductivity and asymmetry are fundamentally contraindicated as electrons fill states directly coupled to the off-centering mechanism (namely, the SOJT effect). Under hole doping, initially the dopants enter nonbonding states, leaving the distortion mostly unperturbed until the Fermi level shifts into the bonding states.

## V. CONCLUSION

We find an asymmetry in the response of the polar distortion in BaTiO<sub>3</sub> under electron doping and hole doping. We proposed a set of analyses to understand the microscopic origin of the behavior and, consistent with previous work, find short-range interactions play a central role in governing local ion off-centering when polarization and metallicity coexist. Specifically, the short-range interaction responsible for driving local off-centering (namely, the SOJT) is disrupted by electrostatic doping via reduction in the magnitude of orbital overlap by changing the occupation of states involved in the covalent bond. Electrostatic doping also results in charge self-regulation, shifting charge from the *B* site to the ligands and opening the band gap. Coulombic interactions are still critical to the stabilization of long-range coordinated off-centering in proper ferroelectrics, however, the local off-centering is primarily stabilized by short-range chemical bonding as described by the SOJT effect. Lastly, although much of the analysis in this paper is particular to SOJT-driven doped ferroelectrics, we anticipate that the metrics developed here may apply well to other materials. In particular, we expect the concept to extend to polar metals, perhaps allowing for greater clarity in comparing and contrasting the different mechanisms for combining polar symmetry and metallicity more generally.

## ACKNOWLEDGMENTS

This project was funded by the Army Research Office (ARO) under Grant No. W911NF-15-1-0017. Calculations were performed using the Quest high-performance computing facility at Northwestern University which is jointly supported by the Office of the Provost, the Office for Research, and Northwestern University Information Technology.

- 
- [1] R. E. Cohen, Origin of ferroelectricity in perovskite oxides, *Nature (London)* **358**, 136 (1992).  
 [2] K. Page, T. Kolodiaznyy, T. Proffen, A. K. Cheetham, and R. Seshadri, Local Structural Origins of the Distinct Electronic Properties of Nb-Substituted SrTiO<sub>3</sub> and BaTiO<sub>3</sub>, *Phys. Rev. Lett.* **101**, 205502 (2008).

- [3] S. Raghavan, J. Y. Zhang, O. F. Shoron, and S. Stemmer, Probing the Metal-Insulator Transition in BaTiO<sub>3</sub> by Electrostatic Doping, *Phys. Rev. Lett.* **117**, 037602 (2016).  
 [4] Y. Wang, X. Liu, J. D. Burton, S. S. Jaswal, and E. Y. Tsybal, Ferroelectric Instability under Screened Coulomb Interactions, *Phys. Rev. Lett.* **109**, 247601 (2012).

- [5] P. Ghosez, X. Gonze, and J.-P. Michenaud, Coulomb interaction and ferroelectric instability of BaTiO<sub>3</sub>, *Europhys. Lett.* **33**, 713 (1996).
- [6] Y. Shi, Y. Guo, X. Wang, A. J. Princep, D. Khalyavin, P. Manuel, Y. Michiue, A. Sato, K. Tsuda, S. Yu, M. Arai, Y. Shirako, M. Akaogi, N. Wang, K. Yamaura, and A. T. Boothroyd, A ferroelectric-like structural transition in a metal, *Nature Mater.* **12**, 1024 (2013).
- [7] P. W. Anderson and E. I. Blount, Symmetry Considerations on Martensitic Transformations: ‘Ferroelectric’ Metals? *Phys. Rev. Lett.* **14**, 217 (1965).
- [8] H. J. Xiang, Origin of polar distortion in LiNbO<sub>3</sub>-type “ferroelectric” metals: Role of A-site instability and short-range interactions, *Phys. Rev. B* **90**, 094108 (2014).
- [9] D. Puggioni and J. M. Rondinelli, Designing a robustly metallic noncentrosymmetric ruthenate oxide with large thermopower anisotropy, *Nat. Commun.* **5**, 3432 (2014).
- [10] T. H. Kim, D. Puggioni, Y. Yuan, L. Xie, H. Zhou, N. Campbell, P. J. Ryan, Y. Choi, J.-W. Kim, J. R. Patzner, S. Ryu, J. P. Podkaminer, J. Irwin, Y. Ma, C. J. Fennie, M. S. Rzchowski, X. Q. Pan, V. Gopalan, J. M. Rondinelli, and C. B. Eom, Polar metals by geometric design, *Nature (London)* **533**, 68 (2016).
- [11] S. Lei, M. Gu, D. Puggioni, G. Stone, J. Peng, J. Ge, Y. Wang, B. Wang, Y. Yuan, K. Wang, Z. Mao, J. M. Rondinelli, and V. Gopalan, Observation of quasi-two-dimensional polar domains and ferroelastic switching in a metal, Ca<sub>3</sub>Ru<sub>2</sub>O<sub>7</sub>, *Nano Lett.* **18**, 3088 (2018).
- [12] H. Zhang, B. Deng, W.-C. Wang, and X.-Q. Shi, Parity-breaking in single-element phases: Ferroelectric-like elemental polar metals, *J. Phys.: Condens. Matter* **30**, 415504 (2018).
- [13] T. Kolodiaznyy, M. Tachibana, H. Kawaji, J. Hwang, and E. Takayama-Muromachi, Persistence of Ferroelectricity in BaTiO<sub>3</sub> through the Insulator-Metal Transition, *Phys. Rev. Lett.* **104**, 147602 (2010).
- [14] F. Cordero, F. Trequattrini, F. Craciun, H. T. Langhammer, D. A. B. Quiroga, and P. S. Silva, Probing ferroelectricity in highly conducting materials through their elastic response: Persistence of ferroelectricity in metallic BaTiO<sub>3- $\delta$</sub> , *Phys. Rev. B* **99**, 064106 (2019).
- [15] J. Fujioka, A. Doi, D. Okuyama, D. Morikawa, T. Arima, K. N. Okada, Y. Kaneko, T. Fukuda, H. Uchiyama, D. Ishikawa, A. Q. R. Baron, K. Kato, M. Takata, and Y. Tokura, Ferroelectric-like metallic state in electron doped BaTiO<sub>3</sub>, *Sci. Rep.* **5**, 13207 (2015).
- [16] H. J. Zhao, A. Filippetti, C. Escorihuela-Sayalero, P. Delugas, E. Canadell, L. Bellaiche, V. Fiorentini, and J. Íñiguez, Meta-screening and permanence of polar distortion in metallized ferroelectrics, *Phys. Rev. B* **97**, 054107 (2018).
- [17] I. B. Bersuker, in *The Jahn-Teller Effect and Vibronic Interactions in Modern Chemistry*, edited by J. P. Fackler, Jr., Modern Inorganic Chemistry (Springer, New York, 2013).
- [18] J. K. Burdett, Use of the Jahn-Teller theorem in inorganic chemistry, *Inorg. Chem.* **20**, 1959 (1981).
- [19] I. B. Bersuker, Pseudo-Jahn-Teller effect—A two-state paradigm in formation, deformation, and transformation of molecular systems and solids, *Chem. Rev.* **113**, 1351 (2013).
- [20] N. Marzari, A. A. Mostofi, J. R. Yates, I. Souza, and D. Vanderbilt, Maximally localized Wannier functions: Theory and applications, *Rev. Mod. Phys.* **84**, 1419 (2012).
- [21] V. Polinger, P. Garcia-Fernandez, and I. B. Bersuker, Pseudo Jahn-Teller origin of ferroelectric instability in BaTiO<sub>3</sub> type perovskites: The Green’s function approach and beyond, *Phys. B* **457**, 296 (2015).
- [22] T. Ishidate, S. Abe, H. Takahashi, and N. Mōri, Phase Diagram of BaTiO<sub>3</sub>, *Phys. Rev. Lett.* **78**, 2397 (1997).
- [23] G. Kresse and J. Furthmüller, Efficient iterative schemes for ab initio total-energy calculations using a plane-wave basis set, *Phys. Rev. B* **54**, 11169 (1996).
- [24] G. Kresse and D. Joubert, From ultrasoft pseudopotentials to the projector augmented-wave method, *Phys. Rev. B* **59**, 1758 (1999).
- [25] J. P. Perdew, A. Ruzsinszky, G. I. Csonka, O. A. Vydrov, G. E. Scuseria, L. A. Constantin, X. Zhou, and K. Burke, Restoring the Density-Gradient Expansion for Exchange in Solids and Surfaces, *Phys. Rev. Lett.* **100**, 136406 (2008).
- [26] P. E. Blöchl, Projector augmented-wave method, *Phys. Rev. B* **50**, 17953 (1994).
- [27] R. H. Buttner and E. N. Maslen, Structural parameters and electron difference density in BaTiO<sub>3</sub>, *Acta Crystallogr., Sect. B: Struct. Sci.* **48**, 764 (1992).
- [28] M. E. Lines and A. M. Glass, *Principles and Applications of Ferroelectrics and Related Materials* (Clarendon, Oxford, 1977).
- [29] Y. Luspin, J. L. Servoin, and F. Gervais, Soft mode spectroscopy in barium titanate, *J. Phys. C: Solid State Phys.* **13**, 3761 (1980).
- [30] R. A. Evarestov and A. V. Bandura, First-principles calculations on the four phases of BaTiO<sub>3</sub>, *J. Comput. Chem.* **33**, 1123 (2012).
- [31] Y. Zhang, J. Sun, J. P. Perdew, and X. Wu, Comparative first-principles studies of prototypical ferroelectric materials by LDA, GGA, and SCAN meta-GGA, *Phys. Rev. B* **96**, 035143 (2017).
- [32] X. He and K.-J. Jin, Persistence of polar distortion with electron doping in lone-pair driven ferroelectrics, *Phys. Rev. B* **94**, 224107 (2016).
- [33] A. Togo and I. Tanaka, First principles phonon calculations in materials science, *Scr. Mater.* **108**, 1 (2015).
- [34] See Supplemental Material at <http://link.aps.org/supplemental/10.1103/PhysRevB.102.014108> for additional soft mode analysis, descriptions of  $r_s$  in different bonding environments, COHP analysis of equatorial bonds, an example of MLWF projection, and analysis of the  $O_{ap} - p(z)$  MLWF under electron doping.
- [35] V. L. Deringer, A. L. Tchougréeff, and R. Dronskowski, Crystal orbital hamilton population (COHP) analysis as projected from plane-wave basis sets, *J. Phys. Chem. A* **115**, 5461 (2011).
- [36] S. Maintz, V. L. Deringer, A. L. Tchougréeff, and R. Dronskowski, LOBSTER: A tool to extract chemical bonding from plane-wave based DFT, *J. Comput. Chem.* **37**, 1030 (2016).
- [37] S. Maintz, M. Esser, and R. Dronskowski, Efficient rotation of local basis functions using real spherical harmonics, *Acta Phys. Pol., B* **47**, 1165 (2016).
- [38] S. Maintz, V. L. Deringer, A. L. Tchougréeff, and R. Dronskowski, Analytic projection from plane-wave and PAW wavefunctions and application to chemical-bonding analysis in solids, *J. Comput. Chem.* **34**, 2557 (2013).
- [39] G. Pizzi, V. Vitale, R. Arita, S. Blügel, F. Freimuth, G. Géranton, M. Gibertini, D. Gresch, C. Johnson, T. Koretsune, J. Ibañez-Azpiroz, H. Lee, J.-M. Lihm, D. Marchand, A.

- Marrazzo, Y. Mokrousov, J. I. Mustafa, Y. Nohara, Y. Nomura, L. Paulatto, S. Poncé, T. Ponweiser, J. Qiao, F. Thöle, S. S. Tsirkin, M. Wierzbowska, N. Marzari, D. Vanderbilt, I. Souza, A. A. Mostofi, and J. R. Yates, WANNIER90 as a community code: New features and applications, *J. Phys.: Condens. Matter* **32**, 165902 (2020).
- [40] A. A. Mostofi, J. R. Yates, G. Pizzi, Y.-S. Lee, I. Souza, D. Vanderbilt, and N. Marzari, An updated version of WANNIER90: A tool for obtaining maximally-localised Wannier functions, *Comput. Phys. Commun.* **185**, 2309 (2014).
- [41] H. Raebiger, S. Lany, and A. Zunger, Charge self-regulation upon changing the oxidation state of transition metals in insulators, *Nature (London)* **453**, 763 (2008).
- [42] R. Kumari, P. K. Kulriya, S. Mishra, V. Kotari, S. N. Achary, A. K. Tyagi, and D. K. Avasthi, Phase-dependent radiation-resistant behavior of BaTiO<sub>3</sub>: An in situ x-ray diffraction study, *J. Am. Ceram. Soc.* **100**, 4263 (2017).